



Article

Hierarchical Ta-Doped TiO₂ Nanorod Arrays with Improved Charge Separation for Photoelectrochemical Water Oxidation under FTO Side Illumination

Shiman He, Yuying Meng ^{*}, Yangfei Cao, Senchuan Huang, Jingling Yang, Shengfu Tong and Mingmei Wu ^{*}

School of Chemistry, Sun Yat-Sen University, No. 135, Xingang Xi Road, Guangzhou 510275, China; heshm3@mail2.sysu.edu.cn (S.H.); caoyf8@mail2.sysu.edu.cn (Y.C.); huangsch3@mail2.sysu.edu.cn (S.H.); yatouguang1@gmail.com (J.Y.); tongshf@mail.sysu.edu.cn (S.T.)

^{*} Correspondence: yymeng9169@gmail.com (Y.M.); ceswmm@mail.sysu.edu.cn (M.W.);
Tel.: +86-020-8411-1823 (Y.M.); +86-020-8411-1823 (M.W.)

Received: 18 October 2018; Accepted: 24 November 2018; Published: 28 November 2018



Abstract: TiO₂ is one of the most attractive semiconductors for use as a photoanode for photoelectrochemical (PEC) water oxidation. However, the large-scale application of TiO₂ photoanodes is restricted due to a short hole diffusion length and low electron mobility, which can be addressed by metal doping and surface decorating. In this paper we report the successful synthesis of hierarchical Ta doped TiO₂ nanorod arrays, with nanoparticles on the top (Ta:TiO₂), on F-doped tin oxide (FTO) glass by a hydrothermal method, and its application as photoanodes for photoelectrochemical water oxidation. It has been found that the incorporation of Ta⁵⁺ in the TiO₂ lattice can decrease the diameter of surface TiO₂ nanoparticles. Ta:TiO₂-140, obtained with a moderate Ta concentration, yields a photocurrent of $\sim 1.36 \text{ mA cm}^{-2}$ at 1.23 V vs. a reversible hydrogen electrode (RHE) under FTO side illumination. The large photocurrent is attributed to the large interface area of the surface TiO₂ nanoparticles and the good electron conductivity due to Ta doping. Besides, the electron trap-free model illustrates that Ta:TiO₂ affords higher transport speed and lower electron resistance when under FTO side illumination.

Keywords: hierarchical TiO₂; Ta doping; charge separation; photoelectrochemical water oxidation

1. Introduction

With the growing demand for energy and the concern of environmental problems worldwide, solar energy has long been regarded as one of the cleanest and renewable energy sources to address these challenges [1]. From an unlimited solar energy perspective, it is highly desirable to convert sunlight into an energy storage medium to provide continuous and stable power. Among sustainable energy systems, photoelectrochemical (PEC) water splitting is an attractive, clean, and environmentally-friendly approach to producing oxygen and hydrogen using sunlight and bias voltage [2]. A key target in PEC research continues to be the development of novel and efficient semiconductor photoelectrocatalysts. TiO₂ has been one of the most promising candidates among various semiconductors since the pioneering work demonstrated by Fujishima and Honda in 1972, because of its chemical stability, cost effectiveness, and nontoxicity [3]. However, TiO₂ still suffers from several challenges for large-scale applications, such as its short minority carrier (hole) diffusion length (10–100 nm) and low electron mobility ($1 \text{ cm}^2 \text{ V}^{-1} \text{ S}^{-1}$). Thus, many efforts have been devoted to addressing these issues [4].

Recent work has been focused on one-dimensional (1-D) nanostructures such as nanotubes, nanowires, and nanorods, since they can improve the charge separation, charge transfer, and light absorption of photoelectrodes [5,6]. The 1-D TiO₂ nanostructure could efficiently transport the charges between the TiO₂ photoelectrode and electrolyte along the axial direction of the nanostructures [7]. However, comparing with nanoparticles, 1-D nanostructures have relatively smaller surface areas, which has a negative impact on the charge transfer process, especially in the case of sluggish anodic water oxidation [8]. Therefore, it is highly desirable to combine the advantage of surface nanoparticles (more surface active sites) and 1-D structures (highly-efficient charge transport along the axial direction) to enhance the overall PEC activity. In addition, doping TiO₂ with other metal elements, such as tantalum, has been widely investigated, as it can tailor the band structure and increase the electric conductivity of TiO₂ [9,10]. Until now, most of the Ta doping TiO₂ nanomaterials have been explored for photocatalysis and dye-sensitized solar cells, while only a few works reported them as photoanodes in PEC water oxidation. Besides, the afforded photocurrents in water splitting have remained quite low over the past few years [10,11]. Typically, TiO₂ PEC cells tested under illumination incident from the F-doped tin oxide (FTO) side (FS illumination) achieve larger current density than those under illumination incident from the TiO₂ side (TS illumination) [12]. However, there is no report on employing the charge injection and separation efficiency to analyze the improved performance for Ta doped TiO₂ photoanodes under FS illumination. Therefore, we believe that investigation of the mechanism of charge injection and separation inside TiO₂ nanostructures under different light illumination models will help us find ways to improve the PEC efficiency of TiO₂-based cells.

In this work, hierarchical Ta doped TiO₂ nanorod arrays, with nanoparticles on the top, on FTO glass (Ta:TiO₂), were synthesized by the hydrothermal method. Ta precursor plays an important role in the formation of the nanoparticles on the top of nanorod arrays. We demonstrate that the efficiency of the TiO₂ nanorod arrays can be improved by surface nanoparticles and Ta doping. Moreover, these materials give a higher photocurrent under FTO illumination than those under TiO₂ illumination, because of the faster electron diffusion and lower charge recombination.

2. Materials and Methods

2.1. Chemicals and Reagents

Hydrochloric acid (HCl 37.5% *w/w*), acetone, absolute ethanol, and *n*-hexane were purchased from Guangdong Guanghua Sci-Tech Co., Ltd. (Guangzhou, China). Tetrabutyl titanate ($\geq 99.0\%$), monopotassium phosphate, dipotassium phosphate, and potassium hydroxide were acquired from the Aladdin Industrial Corporation (Shanghai, China). Sodium sulfite was purchased from the Guangzhou Chemical Reagent Factory (Guangzhou, China). Ta(V) isopropoxide (99.9%, 10% *w/v* in isopropyl alcohol/*n*-hexane) was acquired from Alfa Aesar Co., Ltd. (Waltham, MA, USA). Fluorine-doped tin oxide glass (FTO, 2.2 mm thick, $7 \Omega \text{ cm}^{-2}$, Pilkington) was obtained from the Solar Energy Technology Co., Ltd., Wuhan, China. Deionized water was used throughout the experiment.

2.2. Synthesis of Hierarchical Ta-Doped TiO₂ Nanorod Arrays with Nanoparticles on the Top, on FTO Glass (Ta:TiO₂)

FTO glass was firstly cut into small pieces with a size of 1.5 cm \times 2.0 cm, followed by treatment with sonication in acetone, water, and ethanol for 30 min each step. In a typical synthetic process, 140 μL of Ta isopropoxide (TIO) was dropwise added into an autoclave (15 mL) containing 7 mL of *n*-hexane, 0.7 mL of hydrochloric acid, and 0.7 mL of tetrabutyl titanate (TBT). Then, a piece of FTO substrate was placed into the above autoclave with an angle of 30° against the wall of the Teflon-liner, after which the autoclave underwent solvothermal treatment for 10 h at 180 °C. Once it was cooled to room temperature naturally, the samples were collected and thoroughly rinsed with ethanol and water, separately. After being dried under ambient conditions, the material was annealed in a furnace at 550 °C for 2 h under air atmosphere. Moreover, various materials, denoted as Ta:TiO₂-*v*, where *v*

(0–340 μL) is the volume of Ta isopropoxide (TIO), were obtained to investigate the effect of the TIO amount on PEC activity. In addition, Ta-doped TiO_2 arrays with different lengths (or thickness of the Ta-doped TiO_2 layer) on the substrate were prepared by a similar procedure, with different amounts of TBT (0.3 to 0.8 mL).

The crystalline structure of the materials was measured on an X-ray diffractometer (Rigaku D/max, Tokyo, Japan) operating with a $\text{Cu } K\alpha$ source ($\lambda = 1.5406 \text{ \AA}$) in a 2θ range from 10° to 80° at a scan rate of $10^\circ \text{ min}^{-1}$. X-ray photoelectron spectroscopy (XPS) measurement was performed on a Thermo VG Scientific ESCALAB 250 spectrometer (Waltham, MA, USA) with a monochromatic X-ray source ($\text{Al } K\alpha$). The morphology was verified using a field-emission scanning electron microscope (FESEM, FEI Quanta 400, Hillsboro, OR, USA) operated at 20 kV. A FEI Tecnai G2 F30 transmission electron microscope (Hillsboro, OR, USA) equipped with a high angle annular dark field (HAADF) detector operated at 300 kV was used to obtain the transmission electron microscopy (TEM) images. A Shimadzu UV-3600 spectrophotometer (Kyoto, Japan) equipped with an integrating sphere attachment was chosen to record ultraviolet-visible (UV-Vis) diffuse reflectance spectra using BaSO_4 as the reference.

Photoelectrochemical characterization of Ta-doped TiO_2 photoanodes was carried out on an electrochemical workstation (Metrohm AutoLab PGSTAT302N, Herisau, Switzerland) with a home-built three-electrode optical cell, where the obtained Ta-doped TiO_2 materials, Ag/AgCl , and Pt wire served as working, reference, and counter electrodes, respectively. The linear sweep voltammogram (LSV) curves over different materials were conducted with a scan rate of 20 mV s^{-1} in 1.0 M KOH aqueous solution ($\text{pH} = 13.6$). The illumination source was a 300 W Xe lamp (Perfect light PLS-SXE300CUV, Beijing, China) with an AM 1.5 global filter, calibrated with a standard Si solar cell to simulate AM 1.5 G illumination (100 mW cm^{-2}). Potentials versus (vs.) the reversible hydrogen electrode (RHE) were calculated from the potentials vs. Ag/AgCl using the Nernst equation— $E_{\text{RHE}} = E_{\text{Ag}/\text{AgCl}} + 0.0591(\text{pH}) + 0.196$. Incident-photon-to-current-conversion efficiency (IPCE) was obtained using a solar simulator (Newport 69911 300 W xenon lamp, Irvine, CA, USA) coupled with an aligned monochromator (Oriel Cornerstone 260 1/4 m, Irvine, CA, USA). The electrochemical impedance spectroscopy (EIS) measurement was performed under the open-circuit condition, with 10 mV amplitude in a frequency range from 0.1 to 10 kHz with or without illumination. The donor density was acquired by Mott–Schottky measurement at 1 kHz.

3. Results and Discussion

3.1. Morphology and Structural Characteristics

Figure 1 shows the surface and cross SEM images of Ta: TiO_2 -0 and Ta: TiO_2 -140. The pristine TiO_2 (Ta: TiO_2 -0) consisted of densely packed and vertically aligned nanorods with an average diameter of 150 nm and length of 3 μm . As shown in the cross image of Ta: TiO_2 -140 inserted in Figure 1b, there was no obvious difference in the nanorods' diameter and length in comparison with Ta: TiO_2 -0, while viewed from the surface image, the diameter of the particles on the top of the nanorods was only 40 nm. Therefore, it is highly desirable to deeply investigate the structure of nanoparticles on the top of nanorods to understand the nanorods' growth mechanism. In order to study the precursor's influence on the Ta-doped TiO_2 nanorods' morphology, different amounts of Ta isopropoxide (TIO) were used. The surface and cross SEM images of variable Ta: TiO_2 - v nanorods are shown in Figures S1 and S2, respectively. Figure S1 shows that by increasing the TIO volume from 40 to 190 μL , the size of Ta: TiO_2 nanoparticles on the top of nanorods gradually decreased from 150 to 40 nm. However, the TiO_2 nanoparticles tended to be agglomerated on the nanorods' surface when the TIO volume was further increased above 290 μL . Therefore, TIO must play an important role in the formation of the nanoparticles on the nanorod arrays (Figure 1c) [13]. On the contrary, the increase in TIO had no significant effect on the nanorods' length, remaining consistent at 3 μm for all the Ta: TiO_2 - v materials. Moreover, the Ta:Ti (*at.*%) composition was

investigated via SEM-based energy-dispersive X-ray spectroscopy (EDX), which shows that the Ta content increased with increasing TIO content (Table S1).

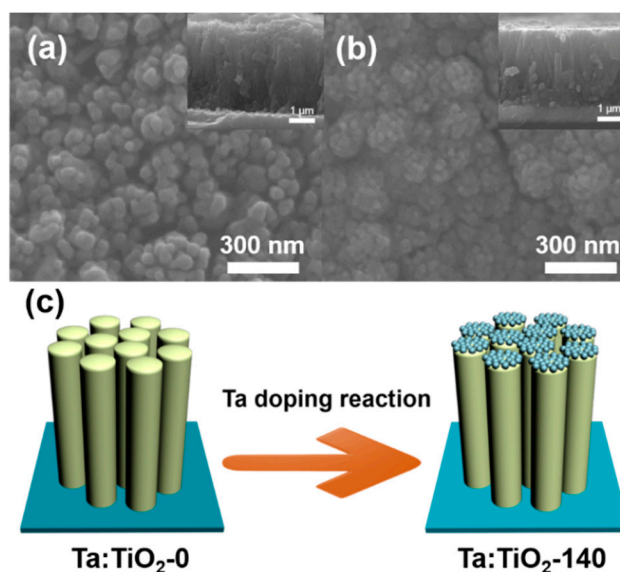


Figure 1. Surface SEM images of (a) Ta:TiO₂-0 and (b) Ta:TiO₂-140. The inserts in (a,b) are the corresponding cross images. (c) The schematic description of the morphology change after the Ta doping reaction.

The crystal structures of Ta:TiO₂-*v* were examined by XRD (Figure 2a). The XRD patterns of all the Ta:TiO₂-*v* materials in Figure 2a show three main diffraction peaks at 27.5, 36.1, and 62.8°, corresponding to the (110), (101), and (002) planes of rutile TiO₂ (#JCPDS 21-1276) [14], respectively. The relatively higher intensity of (002) planes compared with other rutile peaks verifies the TiO₂ nanorods grew in the [001] direction and were highly oriented with respect to the substrate surface [15]. Besides, the diffraction peaks of the FTO substrate were also detected and co-existed with Ta-doped rutile TiO₂. However, the peak at 24.2° of Ta:TiO₂-340 appeared after calcination (Figure 2b), illustrating the existence of Ta₂O₅ due to the excessive TIO. XPS spectra were used to analyze the composition and element states of all the Ta-doped TiO₂ materials. The binding energies were calibrated according to the C 1s peak at 284.8 eV. The typical survey spectra (Figure S3) show four main photoelectron peaks at 458.3, 529.5, 27.3, and 284.8 eV, related with Ti 2p_{3/2}, O 1s, Ta 4f, and C 1s, respectively. The deconvolution of high resolution XPS spectra of Ti 2p, O1s, and Ta 4f are shown in Figure S3 [16]. The presence of the C peak might come from the adsorbed CO₂ species. Figure 2c exhibits the high-resolution spectra of Ti 2p_{3/2}, indicating that the binding energies of Ti 2p peaks for all Ta-doped TiO₂ materials were lower than that of the pristine TiO₂. The reason for this is that the presence of Ta⁵⁺ may bring charge imbalance in the system, which should be equilibrated by the transition of a certain amount of Ti⁴⁺ to Ti³⁺. However, it is well known that Ta₂O₅ cannot shift the Ti 2p peak, suggesting the introduction of Ta⁵⁺ into the TiO₂ lattice [11,16]. Moreover, a 4f_{7/2} peak of Ta was observed at 25.5 eV, revealing the presence of Ta⁵⁺ [17]. As expected, the intensity of the Ta peak increased with the increasing amount of TIO.

Structural characterization of Ta:TiO₂-140 was performed by TEM and high resolution transmission electron microscope (HRTEM). The TEM images of nanorods are shown in Figure S4, which further clearly verify the diameter of TiO₂ nanorods at about 150 nm. Figure 3a displays the low magnification TEM image of the Ta-doped TiO₂ particles cracked from the nanorods after ultrasonic dispersion. The HRTEM image (Figure 3b), measured with the yellow square in Figure 3a, gives a lattice fringe of about 0.325 and 0.249 nm, in agreement with the crystallographic (110) and (101) spacing of rutile TiO₂, respectively [18]. The selected area electron diffraction (SAED) spots of the nanorod (Figure 3c) could be indexed to the (110), (220), and (002) planes, revealing the polycrystalline nature of rutile TiO₂ [19]. Figure 3d demonstrates that Ti, Ta, and O (red square of the nanorod in Figure 3a) were homogeneously distributed through

the whole area, whereas no tantalum oxide was detected by XRD or XPS measurements, which further suggests Ta elements have been successfully incorporated into TiO₂ lattices.

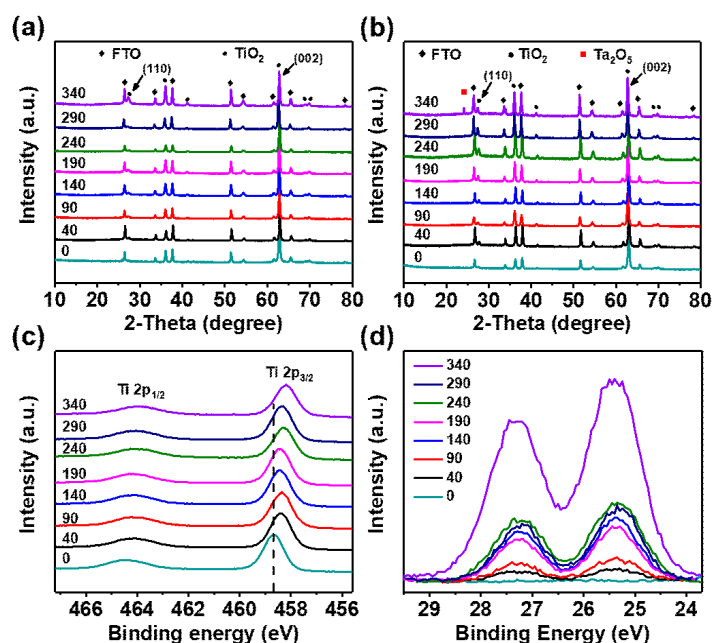


Figure 2. XRD patterns of Ta:TiO_{2-v} materials (a) before and (b) after calcination. High-resolution X-ray photoelectron spectroscopy (XPS) spectra of (c) Ti and (d) Ta for Ta:TiO_{2-v} materials.

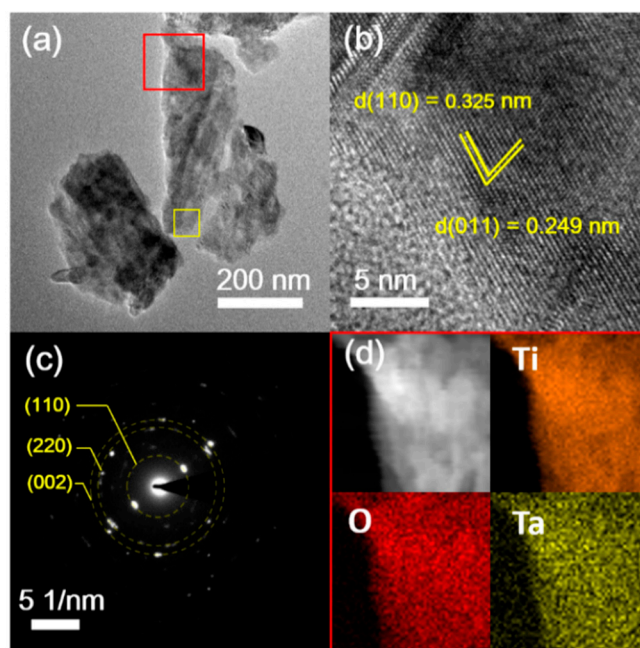
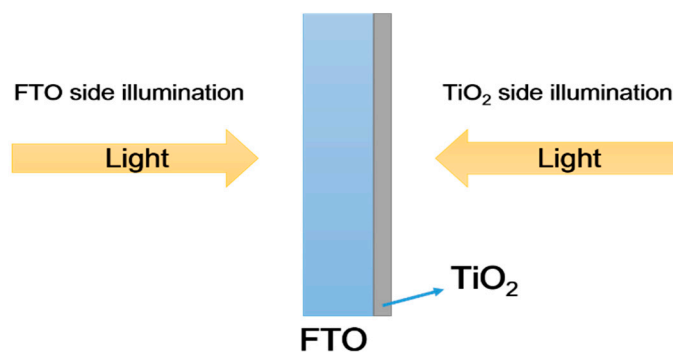


Figure 3. (a) Transmission electron microscopy (TEM), (b) high resolution transmission electron microscope (HRTEM), and (c) selected area electron diffraction (SAED) images of Ta:TiO₂₋₁₄₀. (d) Energy-dispersive X-ray spectroscopy (EDX) mapping data of Ti (orange), O (red), and Ta (yellow).

3.2. Photoelectrochemical Performance

In order to investigate the optimal Ta doping concentration, photoelectrochemical (PEC) properties of Ta:TiO_{2-v} materials were systemically examined in 1.0 M KOH (pH = 13.6) under simulated sun light. Typically, PEC measurements were conducted employing light incident upon both the FTO glass side (FS) and TiO₂ side (TS) (see Scheme 1). Figure 4a,b and Figure S5 show the PEC performance

of all the materials under both TS and FS illumination. With increasing Ta content, the photocurrent density of Ta:TiO₂-*v* firstly increased and then decreased in both cases, giving TiO₂-140 (atomic ratio of Ta to Ti: 0.76 atomic %) the best performance with photocurrent densities of 0.67 and 1.36 mA cm⁻² under TS and FS illumination, respectively. Table S2 shows that the performance of our material is comparable with that obtained with state-of-the-art TiO₂-based photoanodes under TS illumination, and various kinds of photoanodes under FS illumination [11,17,20–27]. However, the photocurrent density decreased drastically when the TIO volume was increased above 290 μL, which may be due to the agglomerated TiO₂ nanoparticles on the nanorods' surface. Specifically, the performance of Ta:TiO₂-340 was even worse than that of pristine TiO₂, because of the surface tantalum oxide generated by the excessive TIO. Figure 4c demonstrates that the improvement in photocurrent under FS illumination can reach up to twice that under TS illumination for Ta:TiO₂-140. According to a previous report, the enhancement of FS illumination was caused by the films' thickness [28]. Therefore, we changed the amount of tetrabutyl titanate in the hydrothermal step to tune the length (thickness) of TiO₂ nanorods. The cross-view of SEM images and the corresponding LSV curves are shown in Figures S6 and S7, indicating that the photocurrent difference between FS-illumination and TS-illumination became smaller with the thickness decrease. Nonetheless, Ta:TiO₂-140 (3 μm) exhibited the highest photocurrent under FS illumination for all series materials with different thicknesses.



Scheme 1. Schematic drawing of Ta:TiO₂-*v* electrode illumination from the F-doped tin oxide (FTO) glass side (FS) and TiO₂ side (TS).

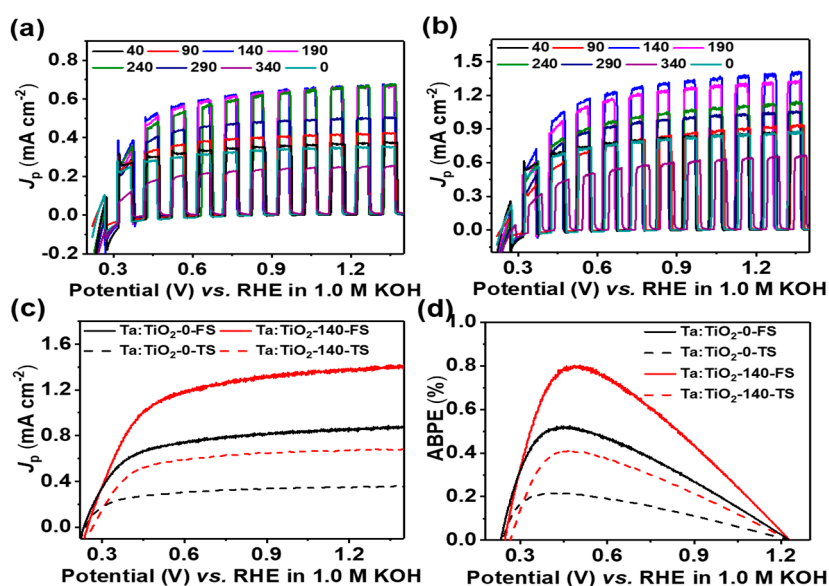


Figure 4. Average chopped linear sweep voltammetry (LSV) curves of Ta:TiO₂-*v* under (a) TS illumination and (b) FS illumination. (c) LSV and (d) applied bias photon-to-current efficiency (ABPE) curves of Ta:TiO₂-0 and -140 under TS and FS illumination.

It is highly desirable to get a higher photocurrent in a relative lower bias region, since this can reduce the external power needed to drive water splitting, and thus increase the overall efficiency of PEC hydrogen generation. The applied bias photon-to-current efficiencies (ABPE, %) of Ta:TiO₂-*v* photoanodes were calculated from the LSV curves in Figure 4c using the following Equation [29]:

$$ABPE = I(1.23 - E)/J_{\text{Light}}, \quad (1)$$

where I is the photocurrent density at the measured bias, E refers to the applied voltage vs. RHE, and J_{Light} is the irradiance intensity of 100 mW cm⁻² (AM 1.5 G). Figure 4d presents the plots of the ABPE as a function of the applied bias. Ta:TiO₂-140 exhibits the highest conversion efficiency of 0.51% under TS illumination and 0.80% under FS illumination at 0.46 V, which is 2.4 and 1.5 times larger than that of Ta:TiO₂-0, respectively. The steady-state photocurrent of Ta:TiO₂-140 was tested at 1.23 V vs. RHE in 1.0 M KOH. It was found that the steady photocurrent densities of FS and TS illumination at 1.23 V were close to the photocurrent density in the LSV curves at the same potential (Figure 4c). Moreover, O₂ bubbles were generated on the surface of Ta:TiO₂-140 under FS illumination throughout the entire examination (Supplementary Video 1), and there was only 2% and 5% current loss for Ta:TiO₂-140 under TS and FS illumination after 3 h continuous reaction, respectively (Figure S8). The stability test was suggestive of the excellent long-term stability and solar conversion application of our photoanodes. To quantitatively investigate the PEC activity, we collected incident-photon-to-current conversion efficiency (IPCE) spectra for Ta:TiO₂-0 and -140 photoanodes at 1.23 V. The IPCE values at the specific wavelengths were calculated according the following equation: $IPCE = (1240 I)/(\lambda \cdot P_{\text{Light}})$, where I is the measured photocurrent density (mA cm⁻²), λ is the wavelength of the incident light (nm), and P_{Light} is the incident light irradiance (mW cm⁻²) [30]. As shown in Figure 5, the maximum IPCE value of Ta:TiO₂-140 was around 62.4% under FS illumination at 360 nm, which was about 1.4 times higher than that of Ta:TiO₂-0. The optimized Ta doping concentration of the TiO₂ could improve the efficiency of the photoelectrodes. The IPCEs of Ta:TiO₂-140 under FS illumination were enhanced significantly compared with the value achieved under TS illumination at the wavelength of 340–400 nm. However, the relatively lower efficiencies at $\lambda < 330$ nm under FS illumination were because of the glass absorption in this wavelength range.

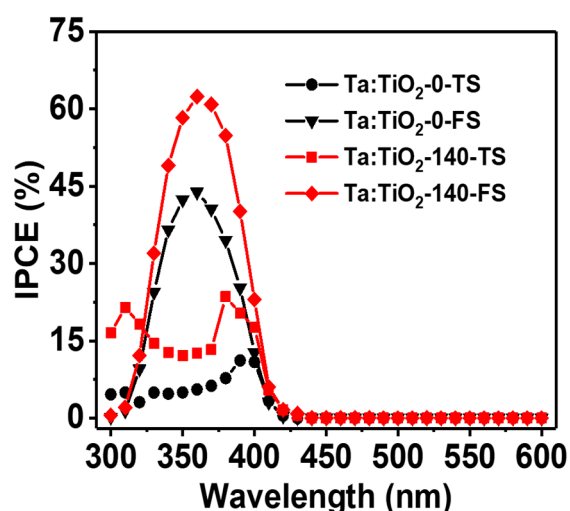


Figure 5. Incident-photon-to-current conversion efficiency (IPCE) of Ta:TiO₂-0 and -140 under TS and FS illumination.

3.3. Charge Separation and Injection Mechanism

To further investigate the reason for the photocurrent enhancement of Ta:TiO₂-140 under FS illumination, three fundamental processes were systemically studied using the following Equation [31]:

$$J_{\text{Wat}} = J_{\text{Abs}} \times \eta_{\text{Injection}} \times \eta_{\text{Separation}} \quad (2)$$

where J_{Wat} is the measured photocurrent density; J_{Abs} refers to the maximum photocurrent density electron flux achievable at the photoanodes; $\eta_{\text{Injection}}$ is the efficiency of photogenerated holes injected from the electrode into the electrolyte for the desired electrochemical reaction, which is also called charge transfer efficiency in some references [31,32]; and $\eta_{\text{Separation}}$ is the photogenerated electron-hole separation efficiency within the material [33]. The light-absorption properties of Ta:TiO₂- v materials were acquired in a wavelength range from 300 to 600 nm (Figure S9), and there was no appreciable difference in light absorption despite the different Ta doping concentrations. The estimated optical bandgaps (E_g) of the materials were extracted from the Tauc plots for direct bandgap transitions (Figure S9b), and the obtained values for all TiO₂ materials were approximately 3.0 eV [34]. Hence, we obtained J_{Abs} by integrating the absorbance across the AM 1.5 G solar spectrum from 300 to 420 nm (Figures S10 and S11, Table S3). The approximate J_{Abs} values indicated that the concentration of Ta doping in our case had no obvious impact on the light absorption.

The separation and injection efficiencies of these photoanodes were obtained via hole-scavenger-assisted PEC measurements (Figure 6a,b). Typically, the photocurrent densities of sulfite oxidation (J_{Sul}) and water oxidation (J_{Wat}) were conducted in 0.5 M potassium phosphate (KH₂PO₄) buffer solution (pH = 7.0) with and without 1.0 M Na₂SO₃ solution, respectively, under FS or TS illumination (Figure S12). $\eta_{\text{Separation}}$ can be determined by the ratio of the photocurrent density of sulfite oxidation to the theoretical maximum photocurrent density, and the results are shown in Figure 6a. It is clearly seen that the separation efficiencies of Ta:TiO₂-140 were higher than those of Ta:TiO₂-0 under both FS and TS illumination. Ta:TiO₂-140 under FS illumination had the highest separation efficiency of 89 % at 1.23 V vs. RHE, which was 1.1 times and 1.5 times higher than those of Ta:TiO₂-0 under FS illumination and Ta:TiO₂-140 under TS illumination, respectively. This can be attributed to the reducing electro-hole recombination in the electrode, which was mostly affected by the conductivity of photoanode. The PEC performance difference of Ta:TiO₂-140 and Ta:TiO₂-0 suggested Ta doping had an important role in decreasing the resistance of TiO₂, which can be beneficial for increasing the separation efficiency. To explain the improvement in separation efficiency between the electrodes measured under FS and TS illumination, trap-free and trap-limited electron transport models reported previously were used [28]. Specifically, regarding FS illumination, the photogenerated electrons will fill most of the trap states to establish a trap-free transport model, since the electrons are generated near the FTO glass side. On the contrary, if the materials are measured under TS illumination, the electrons are generated in the region far from FTO, and most of the electrons should transport a mass of unfilled trap states to FTO. In this case, the trap-limited transport model will form in the zone near FTO, giving rise to a low-speed electron trapping–detrapping process. Obviously, higher electron transport speed decreases the recombination ratio in the electrode, and therefore enhances the separation efficiency.

In addition, the charge injection efficiency was calculated by dividing the photocurrent density of water oxidation into that of sulfite oxidation ($\eta_{\text{Injection}} = J_{\text{Wat}}/J_{\text{Sul}}$), and the results are shown in Figure 6b [35]. The key assumption for this approach is that the surface recombination is negligible, since the consumption of the surface-reaching hole is considered to be 100% using the scavenger (Na₂SO₃) [33]. Ta:TiO₂-140 still exhibited notably higher injection efficiency than that of Ta:TiO₂-0, suggesting the presence of Ta effectively reduced the surface recombination of charge carriers. Moreover, the surface nanoparticles can dramatically increase the contact area between electrode and electrolyte, thus increasing the injection efficiency. On the other hand, the photoelectrodes measured under FS illumination also showed higher injection efficiency than under TS illumination.

The generated electrons can be removed quickly across the trap-free states region of the electrode under FS illumination. Hence, a lower electron accumulation means a lower electron-hole recombination on the surface, and thus a higher injection efficiency of the electrode.

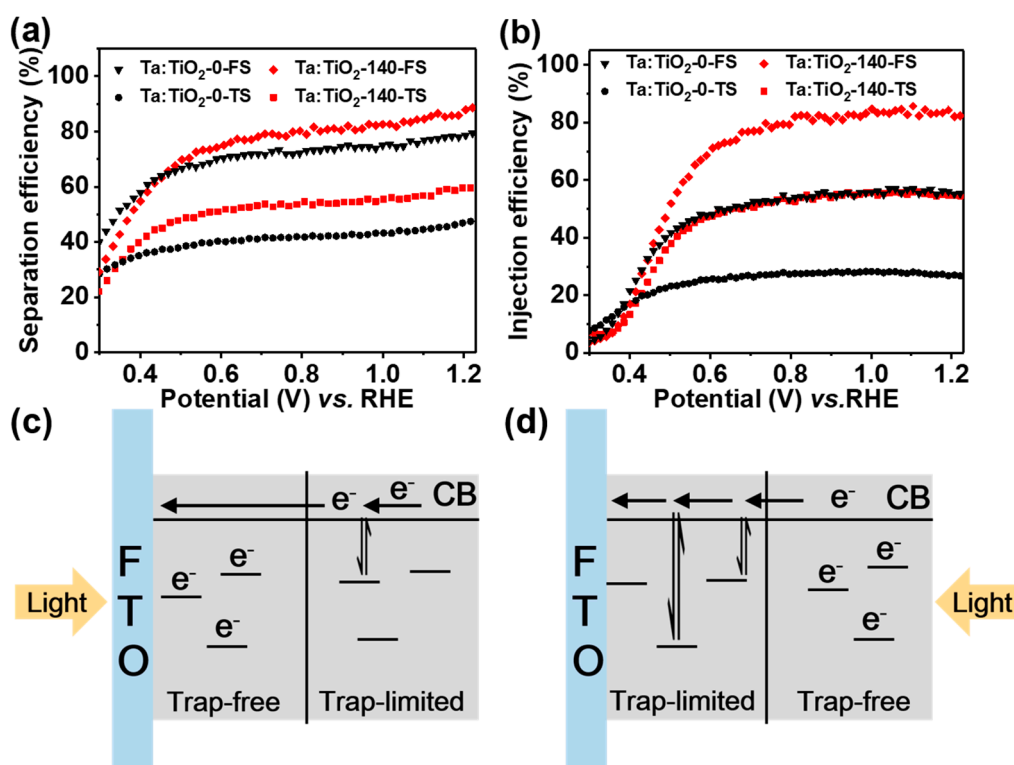


Figure 6. (a) Separation and (b) injection efficiencies of Ta:TiO₂-0 and -140 under TS and FS illumination. (c,d) Schematic illustrating the electron transport behaviors.

3.4. EIS and Band Structure Characteristics

Electrochemical impedance spectroscopy (EIS) curves were measured under the open-circuit condition in the frequency range of 10⁴–0.1 Hz. It is well known that the semicircle at the high frequency zone represents electron transport inside the bulk (R_{CT1}), and the low frequency semicircle is equal to the electrode–electrolyte interface resistance (R_{CT2}) [36]. The diameter of the semicircle in the Nyquist plots reflects the charge transfer resistance, and the large value of impedance elucidates the poor electron conductivity of the photoelectrode [37]. Therefore, the measured EIS raw data (Figure 7a and Figure S13) should be fitted into an equivalent circuit (Figure S14) using Zsimpwin software (the fitted results are shown in Tables S4 and S5). As shown in Figure 7a, the relatively lower resistance of electron transport inside the electrode (R_{CT1}) for the materials using intermediate volume of Ta precursor, especially for Ta:TiO₂-140, indicates the proper Ta doping concentration can accelerate the electron transfer during the reaction. In addition, the low electrode–electrolyte interface resistance (R_{CT2}) of Ta:TiO₂-140 was due to the high contact area of abundant nanoparticles on the top surface, which can promote surface water oxidation [38]. The materials under FS illumination exhibited smaller semicircles than those under TS illumination, implying the trap-free states significantly facilitate the electron transportation inside the electrode, and thus boost the surface water oxidation [39]. These results agree well with the separation and injection efficiencies analysis, as we discussed above.

The Mott–Schottky (M–S) plots were conducted at a fixed frequency (1 KHz). As shown in Figure 7b, the slopes of the linear parts of the curves in the M–S plots were positive, indicating the materials are *n*-type semiconductors. The donor densities (N_D) of Ta:TiO₂-*v* were acquired from the following Equation [40]:

$$N_D = (2/e\epsilon\epsilon_0)/[d(1/C^2)/dV] \quad (3)$$

where C is the space charge layers capacitance, e is the electron charge, ϵ is the dielectric constant, and ϵ_0 is the permittivity of a vacuum. The N_D of Ta:TiO₂-0 and Ta:TiO₂-140 were calculated to be 9.22×10^{19} and $1.69 \times 10^{20} \text{ cm}^{-3}$, respectively. The donor density significantly increases after Ta doping. Therefore, the increased donor density is expected to shift the Fermi level of TiO₂ toward the conduction band, which further facilitates the charge separation at the semiconductor–electrolyte interface, and improves its PEC performance [41]. Besides, the flat band potential (E_{FB}) can be calculated through the intercept of the tangent line in the M–S plots, and the values were determined to be -0.20 and -0.28 V (vs. normal hydrogen electrode, NHE, pH = 0) for Ta:TiO₂-0 and Ta:TiO₂-140, respectively. The gap between the flat band potential and the bottom edge of the conduction band is negligible for n -type semiconductors [42]. Thus, the flat band potential is approximately equal to the conduction band. In our case, no evidence was observed to show a band gap change after Ta doping from the UV-Vis absorption spectra and its corresponding Tauc plot results (Figure S8). Therefore, there must have been some shift of the conduction band edge to complement the valence band edge change, which has been further confirmed by the valence band XPS spectra of Ta:TiO₂-0 and -140 (Figure S15) [9,13,43,44]. The potential energy diagram in Figure 7c illustrates that the conduction band and valence band showed a shift in the cathodic direction by 0.08 V after Ta doping. The negative shift of the conduction band is beneficial for hydrogen production and charge recombination decrease, thus improving the PEC performance [45].

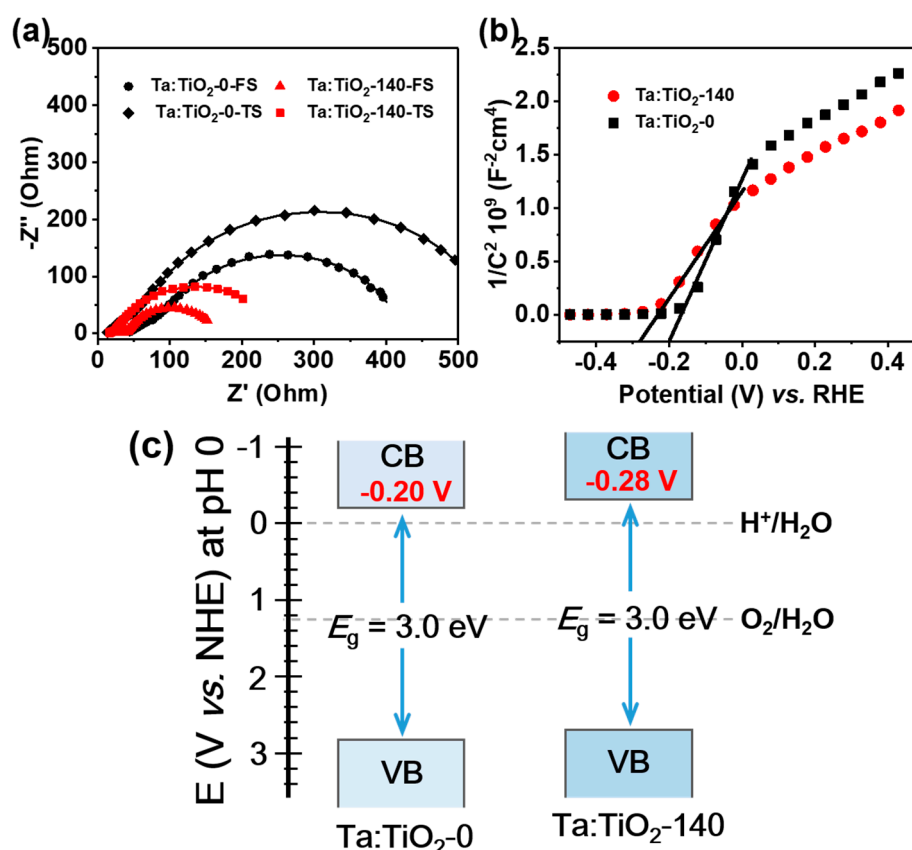


Figure 7. (a) Electrochemical impedance spectroscopy of Ta:TiO₂-0 and -140 under TS and FS illumination. (b) Mott–Schottky plots and (c) band structure diagram of Ta:TiO₂-0 and -140.

4. Conclusions

In summary, we have developed hierarchical Ta doped TiO₂ nanorod arrays, with nanoparticles on the top, on FTO for efficient PEC electrodes. The photoelectrocatalytic activity enhancement of Ta:TiO₂ can be attributed to the following three parameters: Ta doping, surface nanoparticles, and the FS illumination model. Firstly, Ta doping can reduce both bulk and surface electron-hole

recombination by increasing the electron conductivity, as well as upward shift the flat potential to a negative potential. Secondly, the surface nanoparticles on the top of Ta:TiO₂ nanorods effectively increase the interface area between the electrolyte and the active material, thus promoting charge injection and reducing electrode–electrolyte interface resistance. Finally, the electrons have higher transport speed through the trap-free region near the FTO glass under FS illumination, giving higher charge separation efficiency and lower electron transport resistance. Therefore, our work gives a remarkable strategy for designing and constructing low-cost and effective photoanodes for practical sunlight-driven photoelectrochemical water-splitting.

Supplementary Materials: The following are available online at <http://www.mdpi.com/2079-4991/8/12/983/s1>. Figure S1: Surface SEM images of Ta:TiO₂-v, Figure S2: Cross SEM images of Ta:TiO₂-v, Figure S3: (a) XPS survey of Ta:TiO₂-v. The deconvolution of high resolution XPS spectra for (b) O1s, (c) Ti 2P, and (d) Ta 4f of Ta:TiO₂-v, Figure S4: TEM images of Ta:TiO₂-140 nanorods, Figure S5: (a,b) ABPE and (c,d) chopped photocurrent density vs. time of Ta:TiO₂-v under TS illumination and FS illumination, Figure S6: Cross SEM images of Ta doped TiO₂ with different thicknesses (different volume of tetrabutyl titanate), Figure S7: (a) LSV curves, (b) current densities at 1.23 V vs. RHE, and (c) the ratio of J_{FS} to J_{TS} for Ta doped TiO₂ with different thicknesses, Figure S8: Chronoamperometry curves of water oxidation over Ta:TiO₂-140 photoanode at 1.23 V (vs. RHE), Figure S9: (a) UV-Vis absorption spectra and (b) Tauc plots of Ta:TiO₂-v. Figure S10: (a) Diffuse reflectance spectra, (b) transmission spectra, (c) UV-Vis absorption properties (η_{abs}), and (d) the light harvesting efficiencies (η_{LHE}) of Ta:TiO₂-v, Figure S11: (a) Electron flux of AM 1.5 G solar spectrum. (b) Electro flux of Ta:TiO₂-v, Figure S12: LSV curves of Ta:TiO₂-0 and -140 for water oxidation (WO, blue line) measured in 0.5 M phosphate buffer (pH = 7), and sulfite oxidation (SO, red line) measured in 0.5 M phosphate buffer in the presence of 1 M Na₂SO₃ (pH = 7), under TS and FS illumination. The black line was measured in 0.5 M phosphate buffer in the presence of 1 M Na₂SO₃ without illumination, Figure S13: Nyquist plots and magnified Nyquist plots of Ta:TiO₂-v under (a,b) TS illumination and (c,d) FS illumination. The experimental data and simulated impedance response are represented by discrete points and solid lines, respectively, Figure S14: Equivalent circuit used for EIS data fitting. R_s refers to the solution resistance, R_{CT1} is the charge transfer resistance within the electrode, R_{CT2} represents the resistance to electron transport at the electrode–electrolyte interface, CPE is the constant phase angle element, Figure S15: Valence band XPS spectra of Ta:TiO₂-0 and -140, Table S1: SEM-based EDX results for Ta/Ti atomic percentage (%) of Ta:TiO₂-v, Table S2: A summary of recent results of the photocatalytic performance of various photoanodes in photoelectrochemical water oxidation, Table S3: Maximum achievable photocurrent density electron flux of Ta:TiO₂-v, Table S4: The values of R and CPE derived by fitting the EIS of Ta:TiO₂-v under TS illumination, Table S5: The values of R and CPE derived by fitting the EIS of Ta:TiO₂-v under FS illumination, Video S1: Photoelectrochemical testing of Ta:TiO₂-140.

Author Contributions: Conceptualization, S.H. (Shiman He), Y.M., and M.W.; Methodology, S.H. (Shiman He) and S.T.; Formal analysis, Y.C. and S.H. (Senchuan Huang); Data curation, S.H. (Shiman He) and J.Y.; Writing—original draft preparation, S.H. (Shiman He); Writing—review and editing, S.H. (Shiman He), Y.M., and M.W.; Resources, M.W. and Y.M.; Supervision, M.W. and Y.M.

Funding: This research was supported financially by the National Natural Science Foundation of China (NSFC) (51672315, U1702254, 21701199), the Starting Project for Doctoral Fellows Sponsored by the Natural Science Foundation of Guangdong Province (2017A030310503), the Government of Guangdong Province for industry (2017B090917001), the Fundamental Research Funds for the Central Universities of China (17lgpy84), the Government of Guangzhou City for International Joint-project (201704030020), and the Science and Technology Planning Project of Guangdong Province for Industrial Applications (2016B090930001).

Conflicts of Interest: The authors declare no conflict of interest.

References

1. Chen, X.B.; Shen, S.H.; Guo, L.J.; Mao, S.S. Semiconductor-based photocatalytic hydrogen generation. *Chem. Rev.* **2010**, *110*, 6503–6570. [[CrossRef](#)] [[PubMed](#)]
2. Grätzel, M. Photoelectrochemical cells. *Nature* **2001**, *414*, 338–344. [[CrossRef](#)] [[PubMed](#)]
3. Fujishima, A.; Honda, K. Electrochemical photolysis of water at a semiconductor electrode. *Nature* **1972**, *238*, 37–38. [[CrossRef](#)] [[PubMed](#)]
4. Hwang, Y.J.; Hahn, C.; Liu, B.; Yang, P.D. Photoelectrochemical properties of TiO₂ nanowire arrays: A study of the dependence on length and atomic layer deposition coating. *ACS Nano* **2012**, *6*, 5060–5069. [[CrossRef](#)] [[PubMed](#)]
5. Ge, M.; Li, Q.; Cao, C.; Huang, J.; Li, S.; Zhang, S.; Chen, Z.; Zhang, K.; Al-Deyab, S.S.; Lai, Y. One-dimensional TiO₂ nanotube photocatalysts for solar water splitting. *Adv. Sci.* **2017**, *4*, 1600152. [[CrossRef](#)] [[PubMed](#)]

6. Zhan, F.; Liu, W.; Li, H.; Yang, Y.; Wang, M. Ce-doped CdS quantum dot sensitized TiO₂ nanorod films with enhanced visible-light photoelectrochemical properties. *Appl. Surf. Sci.* **2018**, *455*, 476–483. [[CrossRef](#)]
7. Cheng, Q.; Fan, W.; He, Y.; Ma, P.; Vanka, S.; Fan, S.; Mi, Z.; Wang, D. Photorechargeable high voltage redox battery enabled by Ta₃N₅ and GaN/Si dual-photoelectrode. *Adv. Mater.* **2017**, *29*. [[CrossRef](#)] [[PubMed](#)]
8. Yang, J.; Bao, C.; Yu, T.; Hu, Y.; Luo, W.; Zhu, W.; Fu, G.; Li, Z.; Gao, H.; Li, F.; et al. Enhanced performance of photoelectrochemical water splitting with ITO@alpha-Fe₂O₃ core-shell nanowire array as photoanode. *ACS Appl. Mater. Interfaces* **2015**, *7*, 26482–26490. [[CrossRef](#)] [[PubMed](#)]
9. Feng, X.J.; Shankar, K.; Paulose, M.; Grimes, C.A. Tantalum-doped titanium dioxide nanowire arrays for dye-sensitized solar cells with high open-circuit voltage. *Angew. Chem. Int. Ed.* **2009**, *48*, 8095–8098. [[CrossRef](#)] [[PubMed](#)]
10. Gong, Y.Y.; Fu, C.X.; Ting, L.; Chen, J.R.; Zhao, Q.E.; Li, C. Exploring the effect of boron and tantalum codoping on the enhanced photocatalytic activity of TiO₂. *Appl. Surf. Sci.* **2015**, *351*, 746–752. [[CrossRef](#)]
11. Yan, Y.; Lee, J.; Cui, X. Enhanced photoelectrochemical properties of Ta-TiO₂ nanotube arrays prepared by magnetron sputtering. *Vacuum* **2017**, *138*, 30–38. [[CrossRef](#)]
12. Zhou, L.; Yang, Y.; Zhang, J.; Rao, P.M. Photoanode with enhanced performance achieved by coating BiVO₄ onto ZnO-templated Sb-doped SnO₂ nanotube scaffold. *ACS Appl. Mater. Interfaces* **2017**, *9*, 11356–11362. [[CrossRef](#)] [[PubMed](#)]
13. Hoang, S.; Guo, S.W.; Mullins, C.B. Coincorporation of N and Ta into TiO₂ nanowires for visible light driven photoelectrochemical water oxidation. *J. Phys. Chem. C* **2012**, *116*, 23283–23290. [[CrossRef](#)]
14. Yang, X.F.; Chen, J.; Gong, L.; Wu, M.M.; Yu, J.C. Cross-medal arrays of Ta-doped rutile titania. *J. Am. Chem. Soc.* **2009**, *131*, 12048–12049. [[CrossRef](#)] [[PubMed](#)]
15. Liu, B.; Aydil, E.S. Growth of oriented single-crystalline rutile TiO₂ nanorods on transparent conducting substrates for dye-sensitized solar cells. *J. Am. Chem. Soc.* **2009**, *131*, 3985–3990. [[CrossRef](#)] [[PubMed](#)]
16. Bawaked, S.M.; Sathasivam, S.; Bhachu, D.S.; Chadwick, N.; Obaid, A.Y.; Al-Thabaiti, S.; Basahel, S.N.; Carmalt, C.J.; Parkin, I.P. Aerosol assisted chemical vapor deposition of conductive and photocatalytically active tantalum doped titanium dioxide films. *J. Mater. Chem. A* **2014**, *2*, 12849–12856. [[CrossRef](#)]
17. Reitz, C.; Reinacher, J.; Hartmann, P.; Brezesinski, T. Polymer-templated ordered large-pore mesoporous anatase rutile TiO₂:Ta nanocomposite films: Microstructure, electrical conductivity, and photocatalytic and photoelectrochemical properties. *Catal. Today* **2014**, *225*, 55–63. [[CrossRef](#)]
18. Yang, X.F.; Jin, C.J.; Liang, C.L.; Chen, D.H.; Wu, M.M.; Yu, J.C. Nanoflower arrays of rutile TiO₂. *Chem. Commun.* **2011**, *47*, 1184–1186. [[CrossRef](#)] [[PubMed](#)]
19. Yang, X.F.; Zhuang, J.L.; Li, X.Y.; Chen, D.H.; Ouyang, G.F.; Mao, Z.Q.; Han, Y.X.; He, Z.H.; Liang, C.L.; Wu, M.M.; et al. Hierarchically nanostructured rutile arrays. Acid vapor oxidation growth and tunable morphologies. *ACS Nano* **2009**, *3*, 1212–1218. [[CrossRef](#)] [[PubMed](#)]
20. Altomare, M.; Lee, K.; Killian, M.S.; Selli, E.; Schmuki, P. Ta-Doped TiO₂ nanotubes for enhanced solar-light photoelectrochemical water splitting. *Chem.-Eur. J.* **2013**, *19*, 5841–5844. [[CrossRef](#)] [[PubMed](#)]
21. Li, A.; Wang, Z.; Yin, H.; Wang, S.; Yan, P.; Huang, B.; Wang, X.; Li, R.; Zong, X.; Han, H.; et al. Understanding the anatase-rutile phase junction in charge separation and transfer in a TiO₂ electrode for photoelectrochemical water splitting. *Chem. Sci.* **2016**, *7*, 6076–6082. [[CrossRef](#)] [[PubMed](#)]
22. Mao, C.Y.; Zuo, F.; Hou, Y.; Bu, X.H.; Feng, P.Y. In situ preparation of a Ti³⁺ self-doped TiO₂ film with enhanced activity as photoanode by N₂H₄ reduction. *Angew. Chem. Int. Ed.* **2014**, *53*, 10485–10489. [[CrossRef](#)] [[PubMed](#)]
23. Carroll, G.M.; Zhong, D.K.; Gamelin, D.R. Mechanistic insights into solar water oxidation by cobalt-phosphate-modified alpha-Fe₂O₃ photoanodes. *Energy Environ. Sci.* **2015**, *8*, 577–584. [[CrossRef](#)]
24. Zhang, L.W.; Reisner, E.; Baumberg, J.J. Al-doped ZnO inverse opal networks as efficient electron collectors in BiVO₄ photoanodes for solar water oxidation. *Energy Environ. Sci.* **2014**, *7*, 1402–1408. [[CrossRef](#)]
25. Ai, G.J.; Mo, R.; Li, H.X.; Zhong, J.X. Cobalt phosphate modified TiO₂ nanowire arrays as co-catalysts for solar water splitting. *Nanoscale* **2015**, *7*, 6722–6728. [[CrossRef](#)] [[PubMed](#)]
26. Antony, R.P.; Bassi, P.S.; Abdi, F.F.; Chiam, S.Y.; Ren, Y.; Barber, J.; Loo, J.S.C.; Wong, L.H. Electrospun Mo-BiVO₄ for efficient photoelectrochemical water oxidation: Direct evidence of improved hole diffusion length and charge separation. *Electrochim. Acta* **2016**, *211*, 173–182. [[CrossRef](#)]
27. Hong, S.J.; Jun, H.; Borse, P.H.; Lee, J.S. Size effects of WO₃ nanocrystals for photooxidation of water in particulate suspension and photoelectrochemical film systems. *Int. J. Hydrogen Energy* **2009**, *34*, 3234–3242. [[CrossRef](#)]

28. Xiao, S.; Chen, H.; Yang, Z.; Long, X.; Wang, Z.; Zhu, Z.; Qu, Y.; Yang, S. Origin of the different photoelectrochemical performance of mesoporous BiVO₄ photoanodes between the BiVO₄ and the FTO side illumination. *J. Phys. Chem. C* **2015**, *119*, 23350–23357. [[CrossRef](#)]
29. Ye, K.-H.; Chai, Z.; Gu, J.; Yu, X.; Zhao, C.; Zhang, Y.; Mai, W. BiOI-BiVO₄ photoanodes with significantly improved solar water splitting capability: P-n junction to expand solar adsorption range and facilitate charge carrier dynamics. *Nano Energy* **2015**, *18*, 222–231. [[CrossRef](#)]
30. Li, C.; Li, A.; Luo, Z.; Zhang, J.; Chang, X.; Huang, Z.; Wang, T.; Gong, J. Surviving high-temperature calcination: ZrO₂-induced hematite nanotubes for photoelectrochemical water oxidation. *Angew. Chem. Int. Ed.* **2017**, *129*, 4214–4219. [[CrossRef](#)]
31. Cho, I.S.; Lee, C.H.; Feng, Y.Z.; Logar, M.; Rao, P.M.; Cai, L.L.; Kim, D.R.; Sinclair, R.; Zheng, X.L. Codoping titanium dioxide nanowires with tungsten and carbon for enhanced photoelectrochemical performance. *Nat. Commun.* **2013**, *4*, 1723. [[CrossRef](#)] [[PubMed](#)]
32. Kim, T.W.; Choi, K.S. Nanoporous BiVO₄ photoanodes with dual-layer oxygen evolution catalysts for solar water splitting. *Science* **2014**, *343*, 990–994. [[CrossRef](#)] [[PubMed](#)]
33. Yang, W.; Yu, Y.; Starr, M.B.; Yin, X.; Li, Z.; Kvit, A.; Wang, S.; Zhao, P.; Wang, X. Ferroelectric polarization-enhanced photoelectrochemical water splitting in TiO₂-BaTiO₃ core-shell nanowire photoanodes. *Nano Lett.* **2015**, *15*, 7574–7580. [[CrossRef](#)] [[PubMed](#)]
34. Hong, S.J.; Lee, S.; Jang, J.S.; Lee, J.S. Heterojunction BiVO₄/WO₃ electrodes for enhanced photoactivity of water oxidation. *Energy Environ. Sci.* **2011**, *4*, 1781–1787. [[CrossRef](#)]
35. Yang, J.-S.; Wu, J.-J. Low-potential driven fully-depleted BiVO₄/ZnO heterojunction nanodendrite array photoanodes for photoelectrochemical water splitting. *Nano Energy* **2017**, *32*, 232–240. [[CrossRef](#)]
36. Yan, P.L.; Liu, G.J.; Ding, C.M.; Han, H.X.; Shi, J.Y.; Gan, Y.; Li, C. Photoelectrochemical water splitting promoted with a disordered surface layer created by electrochemical reduction. *ACS Appl. Mater. Interfaces* **2015**, *7*, 3791–3796. [[CrossRef](#)] [[PubMed](#)]
37. Shao, M.F.; Ning, F.Y.; Wei, M.; Evans, D.G.; Duan, X. Hierarchical nanowire arrays based on ZnO core-layered double hydroxide shell for largely enhanced photoelectrochemical water splitting. *Adv. Funct. Mater.* **2014**, *24*, 580–586. [[CrossRef](#)]
38. Li, J.; Guo, L.; Lei, N.; Song, Q.; Liang, Z. Metallic Bi nanocrystal-modified defective BiVO₄ photoanodes with exposed (040) facets for photoelectrochemical water splitting. *ChemElectroChem* **2017**, *4*, 2852–2861. [[CrossRef](#)]
39. Tong, X.L.; Yang, P.; Wang, Y.W.; Qin, Y.; Guo, X.Y. Enhanced photoelectrochemical water splitting performance of TiO₂ nanotube arrays coated with an ultrathin nitrogen-doped carbon film by molecular layer deposition. *Nanoscale* **2014**, *6*, 6692–6700. [[CrossRef](#)] [[PubMed](#)]
40. Zhang, Z.H.; Wang, P. Optimization of photoelectrochemical water splitting performance on hierarchical TiO₂ nanotube arrays. *Energy Environ. Sci.* **2012**, *5*, 6506–6512. [[CrossRef](#)]
41. Hou, Y.; Zuo, F.; Dagg, A.P.; Liu, J.K.; Feng, P.Y. Branched WO₃ nanosheet array with layered C₃N₄ heterojunctions and CoO_x nanoparticles as a flexible photoanode for efficient photoelectrochemical water oxidation. *Adv. Mater.* **2014**, *26*, 5043–5049. [[CrossRef](#)] [[PubMed](#)]
42. Dong, Z.; Ding, D.; Li, T.; Ning, C. Ni-doped TiO₂ nanotubes photoanode for enhanced photoelectrochemical water splitting. *Appl. Surf. Sci.* **2018**, *443*, 321–328. [[CrossRef](#)]
43. Chen, X.; Liu, L.; Yu, P.Y.; Mao, S.S. Increasing solar absorption for photocatalysis with black hydrogenated titanium dioxide nanocrystals. *Science* **2011**, *331*, 746–750. [[CrossRef](#)] [[PubMed](#)]
44. He, S.; Meng, Y.; Wu, Q.; Yang, J.; Huang, S.; Li, X.; Tong, S.; Asefa, T.; Wu, M. Ta-doped porous TiO₂ nanorod arrays by substrate-assisted synthesis: Efficient photoelectrocatalysts for water oxidation. *Nanoscale* **2018**, *10*, 19367–19374. [[CrossRef](#)] [[PubMed](#)]
45. Wang, J.; Zhang, W.D. Modification of TiO₂ nanorod arrays by graphite-like C₃N₄ with high visible light photoelectrochemical activity. *Electrochim. Acta* **2012**, *71*, 10–16. [[CrossRef](#)]

